ACS OMEGA

http://pubs.acs.org/journal/acsodf

Article

# Chemical Solution Deposition of Insulating Yttria Nanolayers as Current Flow Diverter in Superconducting $GdBa_2Cu_3O_{7-\delta}$ Coated Conductors

Pedro Barusco,* Xavier Granados, Lavinia Saltarelli, Jean-Hughes Fournier-Lupien, Christian Lacroix, Haifa Ben Saad, Frédéric Sirois, Valentina Roxana Vlad, Albert Calleja, Veit Grosse, Teresa Puig, and Xavier Obradors

Cite This: *ACS Omega* 2022, 7, 15315−15325

Read Online

ACCESS | Metrics & More | Article Recommendations | Supporting Information

**ABSTRACT:** The primary benefit of a metallic stabilization/shunt in high temperature superconductor (HTS) coated conductors (CCs) is to prevent joule heating damage by providing an alternative path for the current flow during the HTS normal state transition (i.e., quench). However, the shunt presence in combination with unavoidable fluctuations in the critical current ($I_c$) of the HTS film can develop a localized quench along the CC's length if the operational current is kept close to $I_c$. This scenario, also known as the hot-spot regime, can lead to the rupture of the CC if the local quench does not propagate fast enough. The current flow diverter (CFD) is the CC architecture concept that has proven to increase the conductor's robustness against a hot-spot regime by simply boosting the quench velocity in the CC, which avoids the shunt compromise in some applications. This work investigates a practical manufacturing route for incorporating the CFD architecture in a reel-to-reel system via the preparation of yttrium oxide ($Y_2O_3$) as an insulating thin nanolayer (~100 nm) on top of a $GdBa_2Cu_3O_7$ (GdBCO) superconductor. Chemical solution deposition (CSD) using ink jet printing (IJP) is shown to be a suitable manufacturing approach. Two sequences of the experimental steps have been investigated, where oxygenation of the GdBCO layer is performed after or before the solution deposition and the $Y_2O_3$ nanolayer thermal treatment formation step. A correlated analysis of the microstructure, in situ oxygenation kinetics, and superconducting properties of the $Ag/Y_2O_3/GdBCO$ trilayer processed under different conditions shows that a new customized functional CC can be prepared. The successful achievement of the CFD effect in the case of the preoxygenated customized CC was confirmed by measuring the current transfer length, thus demonstrating the effectiveness of the CSD-IJP as a processing method.

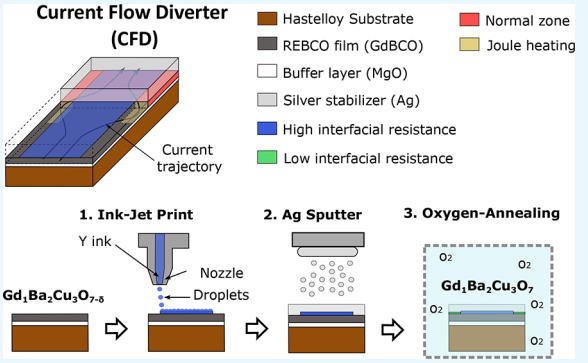


## 1. INTRODUCTION

In the current state of research, second generation (2G) high temperature superconductor (HTS) coated conductors (CCs, also called "tapes") maximize the technical potential of the superconducting properties of $REBa_2Cu_3O_7$ (RE = rare earth or yttrium, REBCO) materials for applications in high-power or high-field devices.[1−3] Some of these devices include the following: motors, generators, transmission cables, high-field magnets, and superconducting fault current limiters (SFCLs).[4−6] Nevertheless, the hot-spot regime is still a pending issue that needs to be addressed before widely extending the use of CCs in practical applications.

Indeed, due to the fabrication process used to deposit and grow the REBCO film on CCs, imperfections in the microstructure, such as grain boundaries associated with misoriented grains, can affect the current percolation within the HTS layer.[7,8] As a result, the distribution of the supercurrents along the length and width of the conductor becomes inhomogeneous, resulting in local variations of the critical current ($I_c$) up to ±10%.[9] If the applied current is near the average $I_c$ of the conductor, zones with lower $I_c$ can locally quench.[10] The quench is characterized by a transition from the superconducting state to the resistive (normal) state. Traditionally, a thin (<2 $\mu$m) continuous coating of silver is deposited on the HTS layer to protect it from atmospheric degradation and provide a low-resistance path for injecting current.[11] This coating also shunts the current from the quenched zone and reduces excessive joule heating. However, owing to the overall low thermal conductivity and the high

Received: September 27, 2021
Accepted: March 15, 2022
Published: April 28, 2022

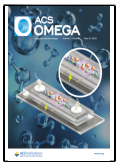

heat capacity of the CCs,[12] these zones can become "hot-spots" due to the slow thermal propagation of the local quench, also referred to as normal zone propagation velocity (NZPV).[13,14] The slow NZPV leads to a local temperature rise capable of damaging the HTS layer, and even of rupturing the conductor.[15] Obviously, the hot-spot regime must be countered to ensure the continuous operation of superconducting devices using 2G HTS CCs.

A straightforward solution to avoid the occurrence of hot-spots is to simply avoid operational current levels too close to $I_c$. However, this approach is impractical in the case of a SFCL, where the operation of the device is based on the natural quench of the CC[16] coming from overcurrents in the power grid. Moreover, it would also represent a significant drawback for the maximum field achievable in high-field superconducting magnets.[3,17]

Currently, the most common solution adopted by CC manufacturers is to reduce joule heating in the hot-spot regime by using a thick metallic shunt stabilizer.[18] Nevertheless, this method makes the SFCL significantly more expensive since it decreases the normal state linear resistance ($\Omega$/m) of the tape, thus requiring longer lengths to maintain the same current limitation threshold in SFCLs.[19,20] In the case of magnets in continuous operation, a thicker shunt can suppress the hot-spot but it further reduces the NZPV to the point of jeopardizing quench detection systems and proper interruption of the power source.[21] In addition, the thick shunt reduces the engineering critical current of the CC, resulting in a reduction of the maximum field intensity achievable by the magnet.

An approach to reduce or even avoid the shunt compromise in SFCLs and magnets is to intentionally increase the interfacial resistance ($\Omega\cdot cm^2$) between the HTS and the metallic shunt in order to increase the current transfer length (CTL).[13,22] This concept has proven that it can boost the NZPV of commercial tapes in a range of 25−100 times.[23] Although effective, this method makes the CC impractical for applications where current leads (current contacts) are required for injecting current. In the leads, the current must travel from the shunt to the REBCO film and the presence of a high interfacial resistance shunt/REBCO can overheat the REBCO film and quench the CC. Therefore, impractically large current contact areas would be required in order to avoid quenching at the current leads.[11] The current flow diverter (CFD) provides a solution to this problem. It was shown experimentally that the CFD concept allows increasing the NZPV on 2G HTS CCs by at least 10 times, while maintaining a relatively low interfacial resistance ($\sim 10^{-7}$ $\Omega\cdot cm^2$) at the current terminals. The CFD architecture[24,25] consists of creating a non-uniform interfacial resistance across the CC's width (Supporting Information (SI) Figure S1). Indeed, the Ag/HTS interface is altered in a way such that the resistance is only increased along the middle of the width of the CC, over its whole length.

Currently, the bottleneck for the industrial acceptance of the CFD as a viable CC architecture resides in the method used to create the high interfacial resistance Ag/HTS. So far, despite its simplicity, the original technique of silver etching and resputtering described in ref 24 is not attractive for the production of CCs in long lengths. Recently, a compatible method to fabricate industrially the CFD CC was proposed using CCs from STI Inc. made with reactive coevaporation and cyclic deposition reaction (RCE-CDR).[26] However, it was shown that the insulator used to implement the CFD, cerium oxide, was degrading the superconducting properties.[27]

The research reported here shows that a scalable CFD architecture can be implemented using a chemical solution deposition (CSD) approach that has been previously used to prepare high-quality functional thin films.[28−30] We show that $Y_2O_3$ nanolayers can be deposited by spin-coating and used to successfully implement the CFD architecture. We also demonstrate that the technique can be scaled to long lengths of CCs via ink jet printing (IJP) in a reel-to-reel system instead of spin-coating. The CSD step was experimentally tested at two different stages in the classical manufacturing sequence of CC fabrication, namely, before and after the oxygenation process of the REBCO layer. The effect of the yttria nanolayer on the CC was evaluated via TEM-EDS/SEM/FIB images, in situ electrical relaxation conductance (ERC) measurements, X-ray diffraction, and scanning Hall probe microscopy (SHPM) magnetization and critical current mappings. Finally, the presence of the CFD was confirmed via current transfer length (CTL) measurements.[31,32]

## 2. EXPERIMENTAL METHOD

**2.1. Film Preparation.** In this work, all 2G HTS CC samples used as a template came from a reel-to-reel manufacturing unit of THEVA.[33] The CC architecture consists of a 100 $\mu$m thick electropolished Hastelloy substrate, on which a 3 $\mu$m thick texturized layer of MgO was evaporated using an inclined deposition technique (ISD),[34,35] and a second 450 nm thick coating of MgO was deposited at a perpendicular angle. Afterward, a 3 $\mu$m thick layer of GdBCO HTS was grown on top of the MgO via electron beam evaporation from a granulate.[33,36] The CC used was not silver coated.

The yttria nanolayers were deposited on top of the GdBCO layer with two CSD processes using yttrium propionate-based precursor solutions. Yttrium acetate ($Y(OAc)_3$) salts were dissolved in a mixture of 26% (v/v) propionic acid ($CH_3CH_2CO_2H$, Aldrich) and 74% (v/v) *n*-butanol in concentrations ranging from 0.01 to 2 M. The solution also included diethanolamine (DEA) in a [Y]/[DEA] molar ratio of 4.5. The solution deposition was initially performed by spin-coating small CC samples (<5 cm) to study the yttria-CFD concept and by IJP in a reel-to-reel system at OXOLUTIA[28,37,38] on 1 m long samples to confirm the industrial scalability. The main objective in both processes (spin-coating and IJP) was to coat about 85−90% of the width (12 mm in the present case) along the surface of the GdBCO films with $Y_2O_3$ to create the CFD pattern. In the spin-coating technique, a mask of the correct size (~1 mm) along the edges of the tape (Figure 1a) was applied to the REBCO film before the spin. In the IJP technique, the same could be done by defining the surface where the droplets were ejected. However, to improve the IJP, a photosensitive UV varnish from Kao-Chimigraf Co.[28,39,40] was introduced to the yttrium propionate solution to increase viscosity and minimize the droplets movement on the surface of the REBCO. IJP was performed using a piezoelectric 512 nozzle Konica Minolta head on which the droplet density of the Y ink was modified near the edges to keep a uniform film thickness through the whole width of the yttria layer. The density of droplets and the ink concentration was selected to obtain a final nanolayer of around 100 nm. The droplet density of the Y ink was reduced by 50% near the edges to avoid the formation of $Y_2O_3$ lips at the edges in the yttria


https://doi.org/10.1021/acsomega.1c05352
ACS Omega 2022, 7, 15315−15325

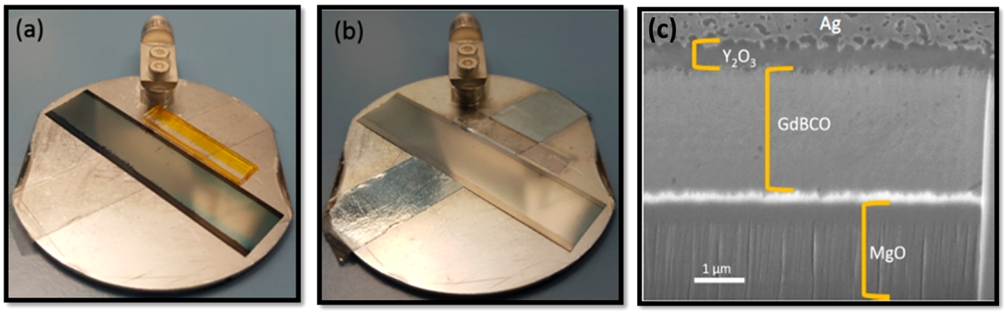


**Figure 1.** (a) Picture of GdBCO CC after IJP of yttria and pyrolysis at 450 °C. The sample is mounted on a metal plate for silver sputtering. (b) Picture of GdBCO CC after silver sputtering. (c) SEM-FIB cross-section of a THEVA CFD-CC deposited with yttria using ink jet printing.

nanolayer (see Figure S2). While lips at the edges could reach up to 5 times thicker than the central part of the layer if all the nozzles were used to generate droplets, this procedure allowed reducing this overthickness to a factor of ∼1.2. The film thickness was determined by cross-section SEM-FIB (Figure 1c) and TEM images (Figure 3).

We prepared 1 m long batches of IJP $Y_2O_3$-CFD layers (Figure S3) at a speed of 35 m/h in a reel-to-reel system. As the CC traveled from reel to reel, the ink was deposited on the REBCO surface and subsequently dried by heating the CC to 50−80 °C with a hovering resistor. Simultaneously to the drying step, the inks were UV cured by means of an array of 10 cm by 25 cm of LEDs with wavelengths between 395 and 405 nm to harden the varnish. In addition, short-length $Y_2O_3$/GdBCO CFD CCs (≤5 cm) were prepared with a SMA spinner 6000 Pro and 0.5 M yttrium propionate solution ($CH_3CH_2CO_2H$/MeOH = 1:1) at 5000 rpm for 2 min on CC samples having polyimide masks on their edges to cover ∼80% of the GdBCO film surface with the solution. Finally, the conversion to $Y_2O_3$ was performed in both cases in a tubular furnace heated at temperatures ranging from 350 to 450 °C (pyrolysis) in oxygen atmosphere for 1 h.[41] The yttria nanolayer thickness was in the range of ∼100 nm, as determined by optical interferometry (Filmetrics, model F20-UV with a spot size in the range of 0.7−1.0 μm). As a final step, the CFD CCs were coated with 500 nm of silver deposited by DC sputtering in a high-vacuum environment ($10^{-7}$ Torr), controlling the temperature below 30 °C. It should be made clear that every experimental result presented here refers to the yttria layer after the pyrolysis process and that using IJP, the yttria deposition should work the same in 12 and 4 mm wide tapes if the coating is kept to 85−90% of the REBCO surface.

**2.2. Oxygenation.** Samples prepared following the first strategy, i.e., starting with non-oxygenated GdBCO layers, were oxygenated after the addition of the yttria and silver layers in order to make the GdBCO layer superconducting. The oxygenation process was initially performed in a tubular furnace with a dry linear oxygen flow of 0.3 cm/s (0.3 L/min). The temperature profile for the oxygen annealing was adapted from THEVA's reel-to-reel system (Figure S4). It started with a ramp up to 600 °C, and the cool down was done in several steps until going back to room temperature.

In a second stage, in order to optimize the oxygenation process while annealing at the lowest possible temperature to avoid interlayer mixing in the Ag/$Y_2O_3$/GdBCO multilayer (particularly silver diffusion), we used a homemade electrical relaxation conductance (ERC) setup that can be used in situ during the oxygenation process. This system allowed investigating the kinetics of oxygen incorporation through the yttria nanolayer at different temperatures in view of implementing a practical oxygenation process for CFD CCs with the shortest possible annealing time. Undoped yttrium oxide ($Y_2O_3$) is a poor oxygen conductor at the typical low oxygenation temperatures of REBCO films; therefore, this overlayer slows down the oxygenation kinetics.

Finally, some CFD CC samples prepared following the second strategy, i.e., starting with oxygenated GdBCO layers, were reoxygenated at 400 °C after adding the yttria coating by CSD and silver coating by sputtering.

**2.3. Microstructural Characterization.** X-ray diffraction patterns of the CFD CCs were obtained using a GADDS diffractometer (Bruker-AXS model D8) equipped with a 2D detector and operating with Cu K$\alpha$ radiation. The surface morphology of the films was analyzed using scanning electron microscopy (SEM FEI Quanta 200 FEG), and the FIB cross-section images were acquired with a dual beam (SEM-FIB) Zeiss 1560 XB apparatus. TEM images of the multilayer cross-section were obtained with a JEOL 2100F apparatus. Cross-section lamellas were obtained with a Hitachi 2000FB FIB, and EDS chemical analyses were performed using an Oxford detector. One of the supports for the lamellas was made of copper; the X-rays emitted by the support overlapped with the copper content in the sample. Therefore, no assertion was done on the basis of the element Cu for the TEM compositional analysis for one sample. The Cu support was later on replaced by one made of aluminum (Al) to avoid this issue.

**2.4. Electrical and Magnetic Characterization.** The superconducting properties in the GdBCO layer were evaluated in a homemade scanning Hall probe measurement (SHPM) system.[42] Samples at different stages of the yttria deposition were field cooled at 77 K with a NdFeB magnet and scanned for acquiring a map of the distribution of the perpendicular trapped magnetic field $B_z$ (Figure S5a). Solving the inverse Fourier problem for $B_z$, we were able to estimate the distribution of the critical current density, $J_c$, as well as the critical current, $I_c$ (Figure S5b). The $I_c$ was calculated by integrating $J_c$ over a virtual close path inside the samples considering the appropriate cross-section area, as described in ref 42.

The presence of the CFD architecture was confirmed by measuring the CTL of the CC using an experimental procedure described in detail in ref 31. The sample was first modified with a chemical etching technique to make a groove on the HTS material along the width of the tape ($y$-axis), thus creating a current path from the HTS to the silver along the tape ($x$-axis) at a specific position across the width (see Figure


https://doi.org/10.1021/acsomega.1c05352
ACS Omega 2022, 7, 15315−15325

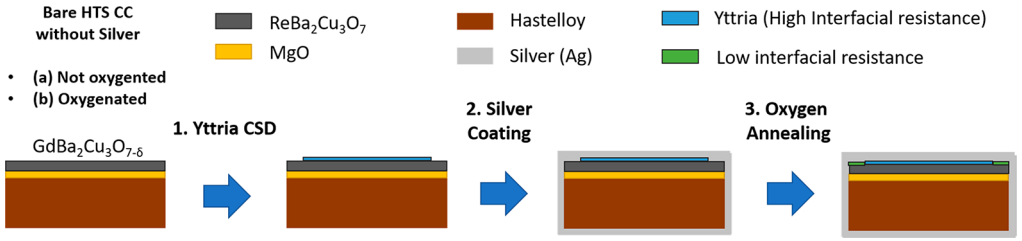


**Figure 2.** General schematics of the experimental steps required to produce a yttria nanolayer and realize the CFD architecture. (a) First route: GdBCO layer not oxygenated initially and this step only performed after the yttria CSD process. (b) Second route: Bare GdBCO layer oxygenated first and then CSD and silver coatings done. Eventually the whole CC may be reoxygenated in a final step.

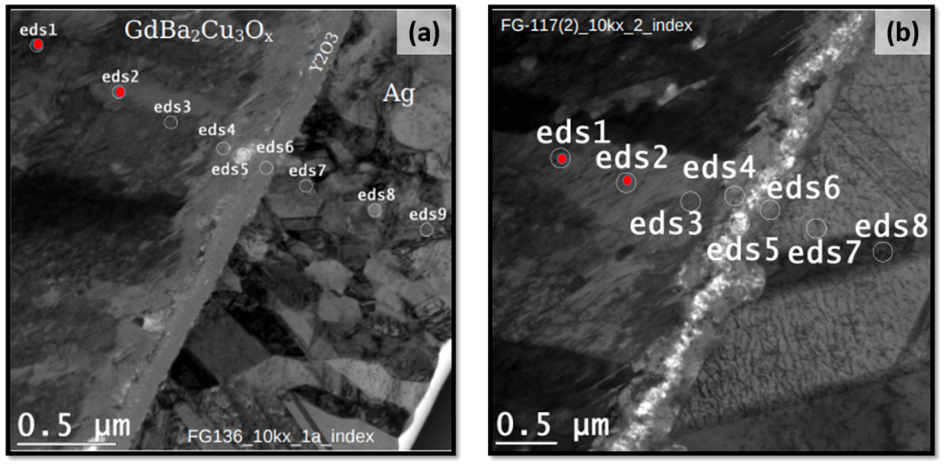


**Figure 3.** TEM images of the $Ag/Y_2O_3/GdBCO$ layers in the CFD architecture for two samples, at two different stages of the first yttria-CFD route: (a) after yttria pyrolysis at 450 °C and silver sputtering (step 2 in Figure 1); (b) after oxygen annealing (step 3 in Figure 1).

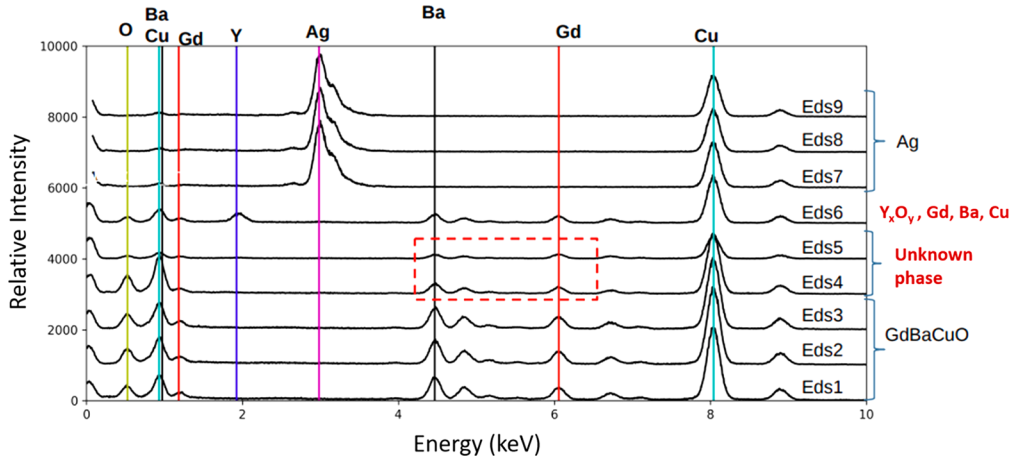


**Figure 4.** EDS spectra for nine points across the $Ag/Y_2O_3/GdBCO$ layers before oxygen annealing (after step 2 in Figure 1). As commented on before in the Experimental Method, the X-rays emitted by the copper support used to create the lamella appears to overlap with the X-rays emitted from the copper contained in the sample.

S6). This path forces the current to transfer to the silver layer of the CC when a low-level transport current is applied to the CC at 77 K. By using arrays of pogo-pins, the surface potential of the sample is measured and the experimental data are fitted with the semianalytical model described in ref 31 to calculate the CTL. The parameters required by this model are (i) the total width of the CC tape ($w$), (ii) the width of the CFD region ($w_f$), (iii) the thickness of the silver shunt ($d$), (iv) the total voltage drop ($\Delta V$) resulting from the etched groove path, (v) the interfacial resistance of the CFD region ($R_f$), and (vi) the interfacial resistance of the CFD-free edges ($R_0$). In the case of a low uniform interfacial resistance across the width where no CFD layer is present ($R_0 = R_f$), the profile of the potential across the width tape is flat (i.e., constant along the tape width).

## 3. RESULTS AND DISCUSSION

The CFD-CCs after yttria deposition and silver sputtering are shown in Figure 1a,b, respectively, and the multilayered architecture can be clearly seen in the SEM-FIB cross-section (Figure 1c) of the CC after the CSD process and silver coating. The yttria deposition by CSD was performed at two different



https://doi.org/10.1021/acsomega.1c05352
ACS Omega 2022, 7, 15315−15325

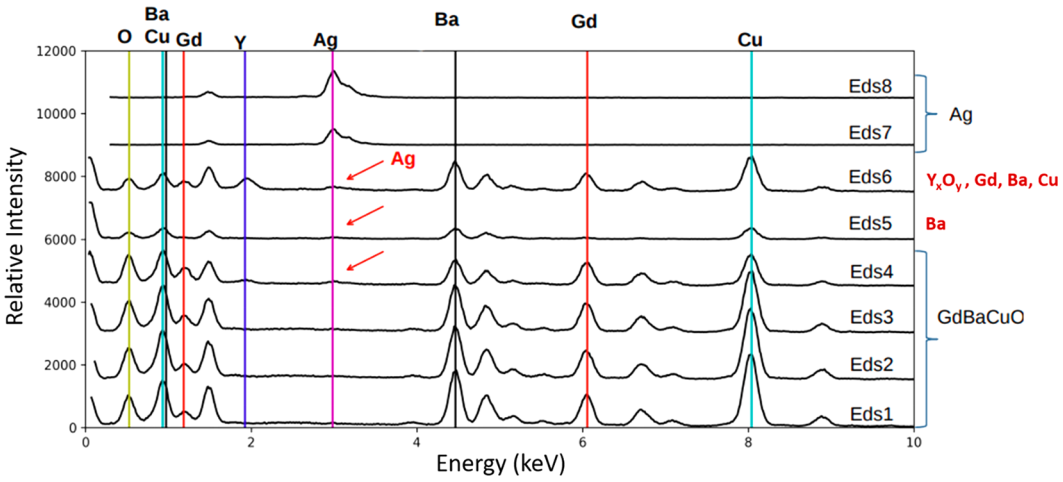


**Figure 5.** EDS spectra for eight points across the $Ag/Y_2O_3/GdBCO$ layers after oxygen annealing (step 3 in Figure 2). As commented on before in the Experimental Method, to avoid the X-rays from a Cu support, the support for this lamella was replaced for one made of aluminum (Al K$\alpha$ peak is 1.486 keV between Gd and Y).

stages of the CC manufacturing process to analyze its suitability to generate CCs with the CFD effect.

In the first route, the CC is neither oxygenated nor silver-coated prior to yttria's deposition. The sequence of experimental steps used for the first yttria-CFD route is illustrated in Figure 2. In step 1, 85−90% of the tape's width (12 mm) is deposited with a yttrium propionate solution via CSD (IJP or spin-coating) and pyrolyzed at 450 °C for 1 h to achieve an amorphous yttria layer (see details in Section 2). In step 2, the tape is silver-coated by sputtering (500−1000 nm). Finally, in step 3, the tape is annealed in 1 bar of oxygen atmosphere to load the necessary oxygen content into the GdBCO film to enable its superconducting properties (Figure S4).

In a second route, the GdBCO CC is oxygenated prior to the yttrium propionate solution deposition and the silver sputtering. The sequence of experimental steps used for this route is the same as that shown in Figure 2. The pyrolysis and annealing temperatures in steps 1 and 3 had to be changed to adapt to certain conditions. The second yttria route, although simpler, creates new technical considerations for the thermal treatments used in the manufacturing steps. For instance, since the tape is oxygenated prior to the yttria IJP deposition, the pyrolysis temperature needs to be reconsidered to avoid the risk of significantly reducing the oxygen content in the GdBCO layer.

The first consideration for the success of the CFD architecture was to ensure the interfacial microstructure of the amorphous yttria after oxygen annealing. For that purpose, TEM images were obtained together with EDS analysis of the $Y_2O_3/GdBCO$ interface fabricated with the first route. Figure 3 shows the $Ag/Y_2O_3/GdBCO$ multilayers for two samples with yttria layers (i) before (Figure 3a) and (ii) after (Figure 3b) oxygen annealing (Figure S4). For the non-oxygenated sample (Figure 3a), nine points across the layers $Ag/Y_2O_3/GdBCO$ were analyzed by EDS (Figure 4). Inside the GdBCO layer, points eds1, eds2, and eds3 reveal an expected rich distribution of Gd, Ba, Cu, and O. They are used here as a baseline for comparison with the other points. In the vicinity of the $GdBCO/Y_2O_3$ interface, points eds4 and eds5 reveal a 100−200 nm region in the GdBCO layer still rich in Gd and Cu but generally depleted in Ba. A similar barium deficiency is seen in eds5. A small diffusion of Y into the GdBCO layer is confirmed in the eds6 analysis for the yttria layer, where we clearly see the Y peak at 2 keV.

Moreover, point eds6 reveals the same counts for Gd, Ba, and Cu in the amorphous yttria. An explanation for this element distribution is the diffusion of Gd, Ba, and Cu toward the yttria layer during the pyrolysis step of the yttria precursor. Nevertheless, silver was found neither in the yttria layer at point eds6 nor in the GdBCO layer at point eds5. Silver is only present in the spectra of points eds7, eds8, and eds9 together with the Cu from the TEM support, as expected, and, since the silver was merely deposited via DC sputtering at low temperatures, it is very unlikely that the Cu diffused toward the silver. This first analysis of a yttria-CFD sample before oxygen annealing confirms the presence of a yttria barrier layer, acting as an interfacial resistance between the silver and the GdBCO film.

Figure 3b shows the TEM cross-section of a fully oxygenated sample heated to 600 °C (Figure S4), indicating the position for eight EDS points across the $Ag/Y_2O_3/GdBCO$ layers. Looking at Figure 3b, it is noticeable that the morphology of the yttria nanolayer changed after the oxygen annealing process. As observed in the EDS spectra of Figure 5, the GdBCO layer (eds1, eds2, and eds3) presents a rich distribution of Gd, Ba, and Cu with some barium deficiency in the vicinity of the $Y_2O_3/GdBCO$ interface (eds4 and eds5). However, eds4 also reveals a small trace of Y close to the $Y_2O_3/GdBCO$ interface, together with some silver. In the expected yttria layer region, eds5 also shows traces of silver but, interestingly, almost no Y nor Gd is found. Moreover, thanks to the Al support, we could confirm the previous assumption that no Cu effectively diffused into the silver layer since no traces of Cu were found in the silver region (eds7 and eds8).

This result reveals that during the oxygenation/annealing process, some silver diffused from the silver metallic shunt through the yttria nanolayer, all the way to the GdBCO layer. A preliminary conclusion would be that the yttria layer is not stable during the oxygen annealing process, allowing a substantial amount of silver to diffuse and thus create a low interfacial resistance with the GdBCO layer, which destroys the CFD effect.



https://doi.org/10.1021/acsomega.1c05352
ACS Omega 2022, 7, 15315−15325

In order to determine the maximum annealing temperature of the Ag/$Y_2O_3$/GdBCO that allows keeping the CFD effect, an electrical relaxation conductance (ERC) experiment was performed. A 12 × 12 $mm^2$ GdBCO sample on which a yttria layer was deposited (corresponding to step 1 in Figure 2) was mounted onto an in situ resistance measurements setup, with four silver wires bonded to the sample's surface in a specific pattern, as shown in Figure 6. Due to the high electrical resistance of yttria, this wire configuration is expected to measure high resistance values (above 100 kΩ). If the silver ink used to attach the silver wires diffuses through the yttria nanolayer because of thermal driving forces during the annealing process, the measured resistance will decrease. After attaching the wires at room temperature, the sample was annealed in an oxygen atmosphere (1 bar) with the temperature profile depicted by the red line in Figure 7, while measuring the electrical resistance.

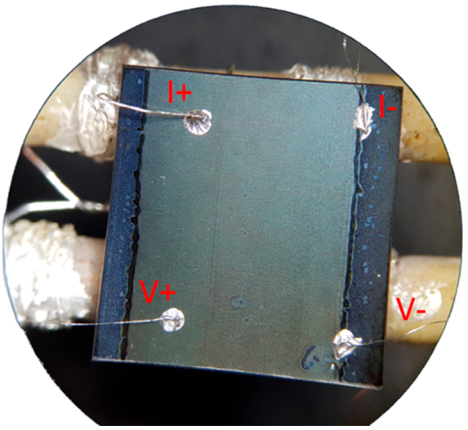


**Figure 6.** Sample of size 12 × 12 $mm^2$ after step 1 (Figure 2) mounted for ERC measurements. One voltage contact ($V^-$) and one current contact ($I^-$) were positioned on top of the GdBCO layer; the other two contacts, $V^+$ and $I^+$ were positioned on top of the yttria layer.

At room temperature, the yttria nanolayer behaved as an insulator providing a global electrical resistance above 100 kΩ. However, the resistance sharply dropped by 2 orders of magnitude as soon as temperature increased to the first 400 °C plateau. Nonetheless, the actual critical drop in resistance only happened after the 500 °C plateau. The resistance dropped below 100 Ω and continuously decreased for 2 h until the 600 °C plateau was reached. Once the temperature stabilized at 600 °C, the resistance stabilized to ∼20 Ω, indicating an electrical connection with the GdBCO layer through the yttria barrier layer. This conclusion is reinforced by comparing the resistance during the 600 °C plateau, before and after the 650 °C plateau (Figure 7). The resistance in both 600 °C plateaus stabilized at the same values, indicating oxygen loading saturation of the GdBCO. After the 650 °C plateau, the remaining temperature plateau corresponded to the resistance readings coming purely from the GdBCO layer. The silver was thus completely "short-circuited" with the GdBCO through the yttria layer.

SEM images of the GdBCO CCs before and after the silver deposition and oxygen annealing confirms that yttria's morphology changed from a dense amorphous layer (Figure 8a) to a sparsely grained crystalline structure (Figure 8b). Furthermore, an X-ray diffraction analysis of a CC CFD sample after the oxygenation heat treatment at 650 °C (in Figure 9) confirms the formation of crystalline body-centered cubic yttrium oxide on top of the GdBCO layer. In Figure 9, the presence of polycrystalline yttria is confirmed while the epitaxial orientation for the GdBCO layer and the inclined MgO (200) epitaxial buffer layer was preserved. This result is in accordance with previous studies,[41,43] in which the onset of crystallization of yttrium propionate was observed to take place between 520 and 550 °C, being nearly completed at 580 °C.

On the basis of the in situ annealing ERC measurements and the XRD spectra, we conclude, therefore, that a thin amorphous yttria nanolayer is unable to electrically insulate the GdBCO from the silver shunt after its phase transition from amorphous to crystalline. The polycrystalline yttria is indeed an electric insulator,[44] but the change in morphology of the yttria layer allows silver to diffuse across the yttria layer and therefore compromises the high interfacial resistance Ag/GdBCO required to achieve the CFD effect. In order to

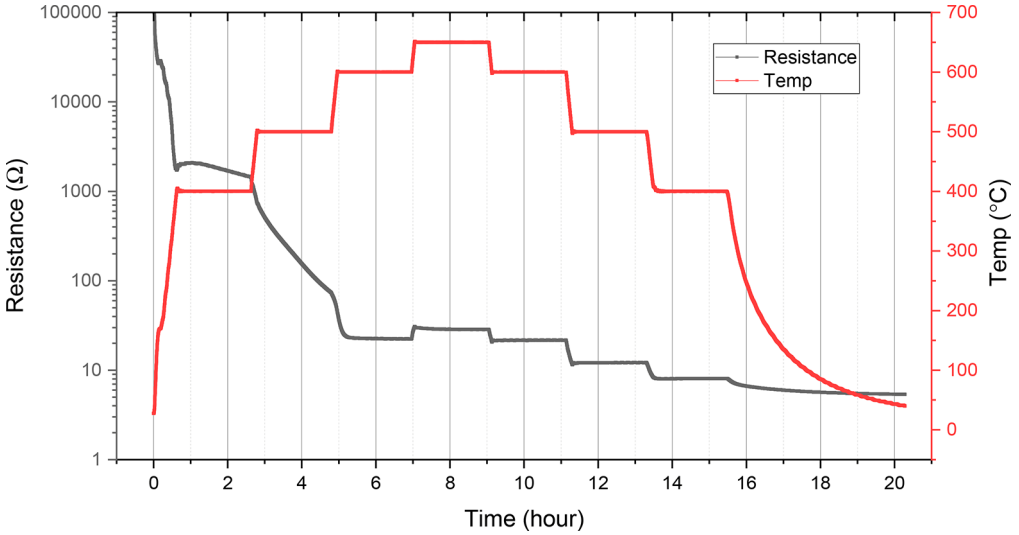


**Figure 7.** In situ electrical conductivity relaxation (ECR) measurements of the yttria nanolayer on GdBCO substrate during oxygen annealing at different temperature dwells.



https://doi.org/10.1021/acsomega.1c05352
ACS Omega 2022, 7, 15315−15325

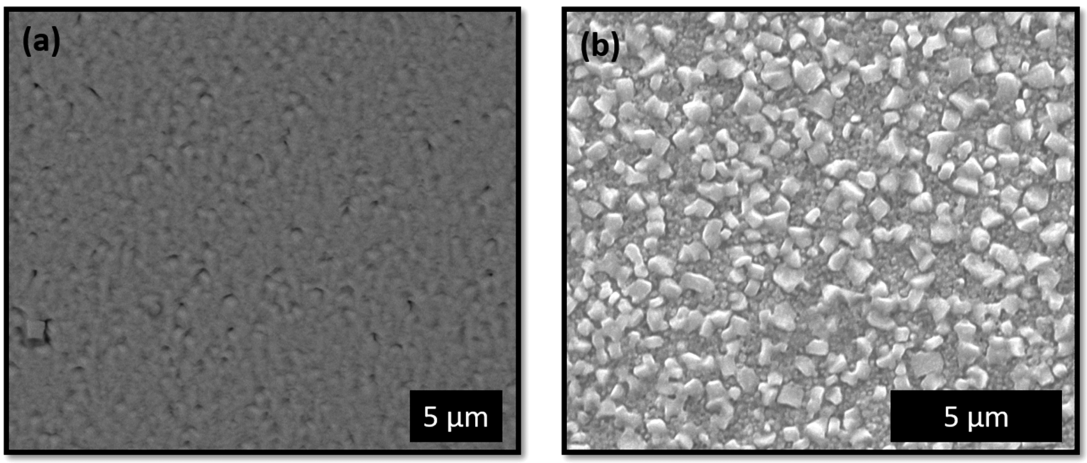


**Figure 8.** SEM images showing (a) dense amorphous yttria layer on top of the GdBCO after yttria pyrolysis at 450 °C and (b) spare crystalline formation on top of the GdBCO substrate after ERC in- itu resistance measurements reaching 600 °C.

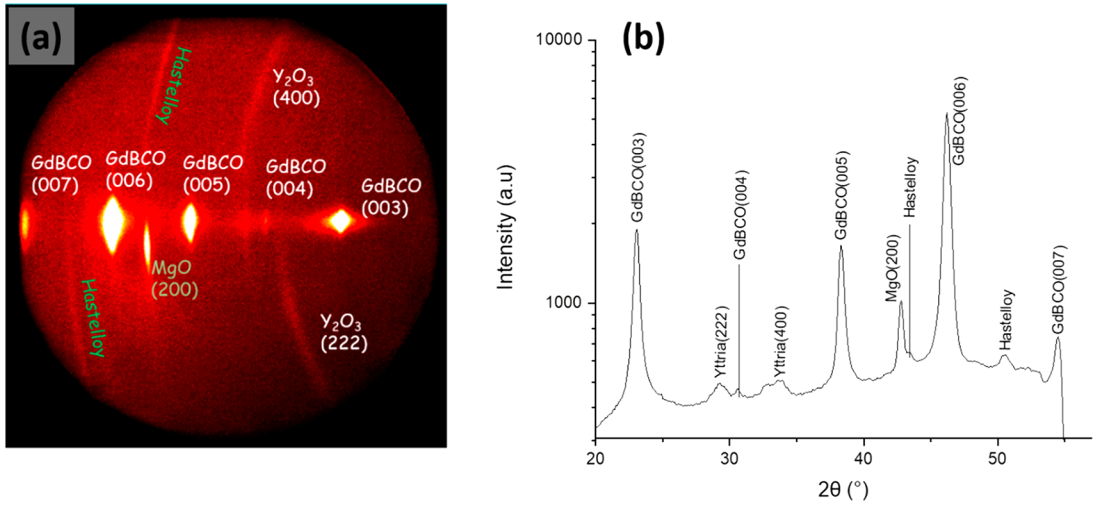


**Figure 9.** (a) GADDS X-ray diffraction of layered sample $Y_2O_3$/GdBCO/MgO/Hastelloy after oxygen annealing. (b) Integrated $\theta$−$2\theta$ X-ray diffraction pattern. A crystalline epitaxial structure of GdBCO plus an inclined MgO (200) epitaxial layer are observed. The rings at $2\theta$ = 43.5° and 50.9° correspond to the Hastelloy substrate. The presence of polycrystalline yttria is confirmed by the (400) and (222) peaks at $2\theta$ = 29.15° and 33.8°, respectively.

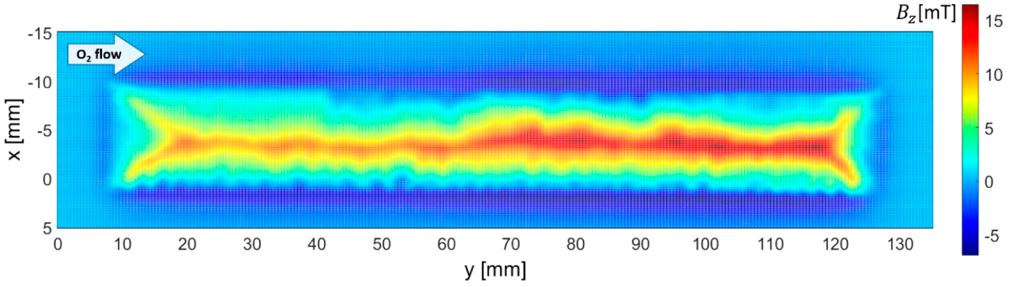


**Figure 10.** Perpendicular trapped field, $B_Z$, measured by scanning Hall probe microscopy (SHPM) for a 110 × 12 mm$^2$ CC with 91 nm thick yttria and 1 $\mu$m thick silver. The sample was oxygenated in a tubular furnace at 450 °C for 48 h with a low oxygen flow of 0.03 L/min of 1 bar. Comparison with a fully oxygenated sample is included in the SI Figure S5.

maintain the yttria in the amorphous phase during oxygenation, the temperature should not exceed ∼500 °C.

Therefore, the possibility of oxygen annealing the $Y_2O_3$/GdBCO bilayer below 500 °C was tested in different samples for a variety of profiles. The subsequent evaluation of these profiles was performed by measuring the perpendicular trapped field $B_z$ after field cooling the samples in liquid nitrogen.[42,45] Unfortunately, for all temperature profiles below 500 °C, the inhomogeneous distribution of $B_z$ indicated an incomplete oxygen loading of the GdBCO layer. This temperature limitation is illustrated by the $B_z(x,y)$ map in Figure 10, where a 110 × 12 mm$^2$ CC sample was oxygen annealed in a single temperature step of 450 °C for 48 h. Even after 48 h, the homogeneity across the width ($x$-axis) and the length ($y$-axis)



https://doi.org/10.1021/acsomega.1c05352
ACS Omega 2022, 7, 15315−15325

Table 1. $B_z$ Distribution Comparison of Three 12 × 50 mm$^2$ GdBCO THEVA Tape Samples before and after Yttria Nanolayer Formation (Pyrolysis) and after Additional Silver Sputtering and Oxygen Annealing at Three Different Temperatures: 350, 400, and 450 °C[a]

| virgin sample without silver (before pyrolysis) | | | after yttria pyrolysis | | after yttria pyrolysis, silver sputtering, and oxygen annealing | |
|---|---|---|---|---|---|---|
| av field $B_z$ (mT) | $I_c$ (A) | pyrolysis and annealing (°C)[b] | av field $B_z$ (mT) | $I_c$ (A) | av field $B_z$ (mT) | $I_c$ (A) |
| 41.2 ± 19 | 505 ± 29 | **350** | 19.8 ± 33 | 242 ± 49 | 30.3 ± 23 | 371 ± 23 |
| 42.1 ± 25 | 517 ± 35 | **400** | 20.3 ± 38 | 249 ± 53 | 32.0 ± 21 | 392 ± 29 |
| 41.8 ± 27 | 513 ± 37 | **450** | 21.1 ± 58 | 245 ± 79 | 29.4 ± 35 | 360 ± 49 |

[a]All samples were coated with 500 nm of silver before the oxygen annealing. [b]Bold values represent the sample in the previous Hall-scan figure.

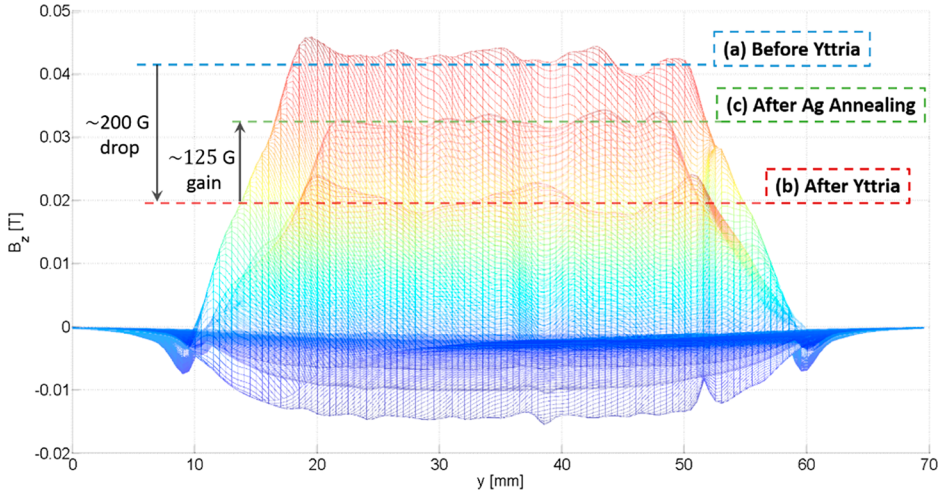


**Figure 11.** Longitudinal $B_z$ distribution comparison of a 12 × 50 mm$^2$ GdBCO CC, before (a) and after (b) depositing and pyrolyzing the yttria layer at 400 °C and subsequent (c) deposition of 500 nm of silver and oxygen annealing at 400 °C.

was unsatisfactory for performing transport current tests. Below 500 °C, all samples annealed in oxygen for less than 24 h presented a clear deficiency of $B_z$ in the region covered with the yttria (Figure S7). In other words, it was concluded that the oxygen diffuses fast at the edges of the CC where no yttria layer exists, as it is seen in the SHPM figure where magnetization signal is only seen in the edges (Figure S7). Even though having the diffusion, $D$, along the $ab$-planes, much faster than the diffusion along the $c$-axis ($D_{ab} \gg D_c$), theoretically, it would take days for the oxygen to complete the bulk diffusion across the whole tape width starting from both yttria-free edges. We hence concluded that the fastest oxygenation path is still through the yttria layer followed the vertical direction and then along the a−b plane, similarly as in bare YBCO films.[46]

The second strategy to achieve a fully doped GdBCO layer in a practical time frame without compromising the CFD effect of the yttria nanolayers was to anneal the CC in oxygen prior to the CSD step. This route was envisioned to avoid the need of reoxygenating the GdBCO layer after the deposition of the yttrium propionate solution and pyrolysis. For this reason, a bare 15 cm long GdBCO CC sample was oxygenated prior to preparation of the yttria nanolayer on top in order to reach a high critical current, which was confirmed by SHPM (see Table 1). The 15 cm sample was then cut in three 50 mm long pieces. Each 50 mm long sample was coated with a yttrium propionate solution via spin-coating to produce the CFD geometry and then pyrolyzed at a specific temperature (one sample at 350 °C, a second sample at 400 °C, and the third last one at 450 °C). Afterward, all samples were sputtered with 500 nm of silver and annealed in oxygen using the same temperature profile used in the pyrolysis. In Figure 11, we show a comparative $B_z$ mapping before (a) and after (b) the yttria CSD formation process and silver sputtering and oxygen annealing at 400 °C for 3 h. After the yttria nanolayer formation, the average field (and $I_c$) dropped by more than 50%, and the amplitude variations of $B_z$ (inhomogeneities) increased up to 15%. The trapped field results measured by SHPM for all samples are shown in Table 1.

However, in all samples, the subsequent silver deposition and oxygen annealing after the yttria CSD process significantly increased the magnetization values and reduced the inhomogeneity. This result can be seen in the last two columns of Table 1. No direct correlation between annealing temperature and final $I_c$ can be firmly established since $I_c$ ± error values of the different samples are overlapped due to variations in the magnetization. In Figure 11, we show that the highest magnetization recovery happened for the sample with the yttria nanolayer and additionally annealed at 400 °C for 3 h after silver deposition.

As one can observe, the CSD process of yttria nanolayer formation reduces the oxygen content of the GdBCO film, also confirmed by the observed reduction of $T_c$ and the reduced transition sharpness in low magnetic field susceptibility measurements performed by SQUID magnetometry (Figure S8). Nevertheless, since the pyrolysis step and the oxygen annealing after silver deposition were both executed with the same temperature profile, seeing the increase in magnetization after silver annealing illustrates how the silver plays a vital role in the oxygen in-diffusion of the GdBCO layer.[46,47] We suggest that the silver layer deposited at the yttria surface has a catalytic effect accelerating the diffusion of oxygen into the


https://doi.org/10.1021/acsomega.1c05352
ACS Omega 2022, 7, 15315−15325

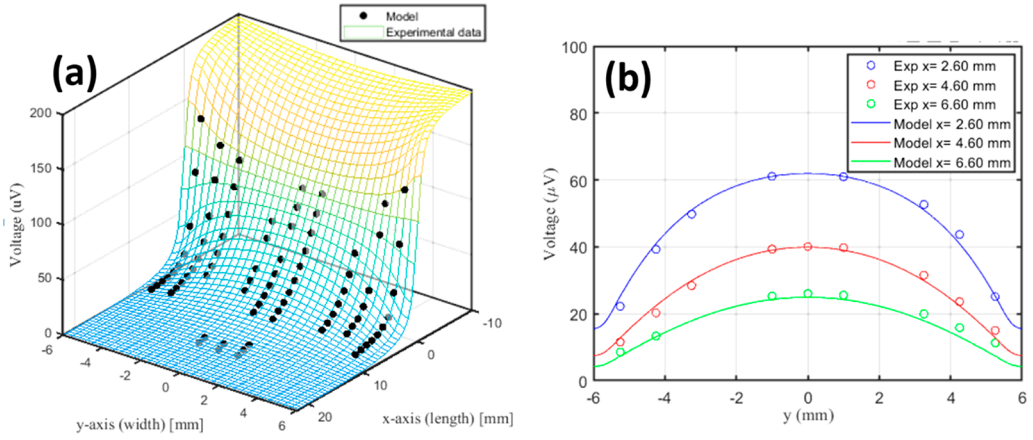


**Figure 12.** Current transfer length (CTL) measurements for a typical CFD sample at 77 K. (a) Experimental data and fitted model of the potential distribution on the surface of the sample. (b) Parabolic potential distribution along the width ($y$-axis) of the sample.

GdBCO layer, as it has been previously demonstrated in YBCO films.[48,49]

In order to confirm the CFD effectiveness of the CC with the amorphous yttria nanolayer after pyrolysis and oxygen annealed at 400 °C, the current transfer length (CTL) of the sample shown in Figure 11 was measured following the procedures described in detail in ref 31. Essentially, the voltage profile along $x$-axis and across $y$-axis on the surface of the tape is measured for a constant transport current crossing the sample. The experimental data and the 2D potential surface distribution model are shown in Figure 12a. In the case of a uniform interfacial resistance, the voltage distribution across the CC's width ($y$-axis) should be constant, but a straightforward look at the potential distribution across the width for different planes along the length, reveals the parabolic voltage distribution characteristic of the non-uniform interfacial resistance in the CFD architecture.[32] Following the fitting process described in ref 31, the best fitting for potential surface is found for the parameters $\Delta V = 200$, $w_f = 11$ mm, $w = 12$ mm, $d = 1$ $\mu$m, $R_0 = 10^{-5}$ Ω·cm$^2$, and $R_f = 10^{-3}$ Ω·cm$^2$. The parameters $w_f$, $w$, and $d$ are coherent with real dimensions of the CC (tape width, CFD width and Ag shunt thickness) and, $\Delta V$, $R_0$ and $R_f$, are in the expected range for the interfacial resistances involved. These parameters lead to a current transfer length of $\lambda = 3.26$ mm, which is bigger than the expect CTL for a CC with uniform interfacial ($R_0 = R_f$) resistance in the $10^{-7}$ Ω·cm$^2$ range, and agrees with the CTL values found for CFD samples created in a previous study with the resputtering silver method.[24,32]

This fit suggests that the interfacial resistance along the yttria CFD edges is possibly greater than the desired values of $10^{-7}$ Ω·cm$^2$. Applying the formula $R_i \approx R_0/(1-f)$ from ref 24, the overall interfacial resistance ($R_i$ is estimated to be $10^{-4}$ Ω·cm$^2$. This value, as discussed in ref 11, is in the limit for maintaining a practical current contact size for tapes operating in continuous current transport above 500 A. Transport current measurements should be performed with longer samples at this level of current to confirm the presence of joule heating. If the interfacial resistance is indeed high, a slight increase in the annealing temperature during oxygenation should decrease the interfacial resistance[11] and hence allow the conductor to operate above ~500 A.

## 4. CONCLUSION AND OUTLOOK

Yttria nanolayers were deposited via CSD on bare GdBCO CCs (not silver coated after manufacturing) to create a $Y_2O_3$/GdBCO bilayer pattern capable of producing the CFD effect (~80% of insulating interface) in the manufacturing steps of commercial CCs. The first attempt consisted of performing oxygen annealing of the bilayer after silver coating. However, this approach seems to be impractical due to temperature restrictions regarding the compatibility of the GdBCO and yttria. Above 500 °C, the silver diffuses through the yttria layer during oxygen annealing and, below 500 °C, we generate unacceptable $I_c$ fluctuations due to inhomogeneous oxygen in-diffusion in the GdBCO film. In a second attempt, CCs samples were annealed in oxygen prior to depositing the yttria layer by CSD, with the hope of minimizing deoxygenation of the GdBCO film. According to the SHPM analysis, the yttria deposition by CSD reduces $I_c$ by ~50%. However, additional oxygen annealing after the silver deposition allows recovering $I_c$ to ~75% of its original value, thus essentially validating the potential of this CFD processing approach. Finally, the CFD effect was confirmed via CTL measurements following a special experimental procedure that determines the non-uniform voltage potential distribution across the insulating nanolayer of yttria.

The expected boost in the NZPV associated with the yttria nanolayer and CFD effect will be confirmed after the fabrication of long-length CC samples (>10 cm) and electrical transport current tests. These future NZPV tests should reveal if the estimated total interfacial resistance of $10^{-4}$ Ω·cm$^2$ is a limiting factor when the transport current is in the range of 500 A. The amount of joule heating at the current terminals will be the determining factor to conclude about the ability of the CSD-deposited yttria layer to behave as a practical CFD layer for HTS CCs.

## ■ ASSOCIATED CONTENT

### Supporting Information

The Supporting Information is available free of charge at https://pubs.acs.org/doi/10.1021/acsomega.1c05352.

Illustration of the CFD concept; images of the inkjet printing process performed by OXOLUTIA SL; temperature profile used by THEVA GmbH for oxygenation; scanning Hall probe microscopy images of 12 mm wide HTS tapes; description of the current transfer length



https://doi.org/10.1021/acsomega.1c05352
ACS Omega 2022, 7, 15315−15325

experiment; SQUID magnetometry measurements for the yttria-CFD (PDF)

## AUTHOR INFORMATION


### Corresponding Author

**Pedro Barusco** − *Institut de Ciència de Materials de Barcelona (ICMAB-CSIC), 08193 Bellaterra, Catalonia, Spain;* orcid.org/0000-0003-3172-4354; Email: pbarusco@icmab.es, pebarusco@gmail.com

### Authors

**Xavier Granados** − *Institut de Ciència de Materials de Barcelona (ICMAB-CSIC), 08193 Bellaterra, Catalonia, Spain*

**Lavinia Saltarelli** − *Institut de Ciència de Materials de Barcelona (ICMAB-CSIC), 08193 Bellaterra, Catalonia, Spain*

**Jean-Hughes Fournier-Lupien** − *Polytechnique Montréal, Montréal, Québec, Canada H3T 1J4*

**Christian Lacroix** − *Polytechnique Montréal, Montréal, Québec, Canada H3T 1J4*

**Haifa Ben Saad** − *Polytechnique Montréal, Montréal, Québec, Canada H3T 1J4*

**Frédéric Sirois** − *Polytechnique Montréal, Montréal, Québec, Canada H3T 1J4*

**Valentina Roxana Vlad** − *Institut de Ciència de Materials de Barcelona (ICMAB-CSIC), 08193 Bellaterra, Catalonia, Spain*

**Albert Calleja** − *OXOLUTIA SL, 08210 Barberà del Vallès, Catalonia, Spain*

**Veit Grosse** − *THEVA Dünnschichttechnik GmbH, 85737 Ismaning, Germany*

**Teresa Puig** − *Institut de Ciència de Materials de Barcelona (ICMAB-CSIC), 08193 Bellaterra, Catalonia, Spain*

**Xavier Obradors** − *Institut de Ciència de Materials de Barcelona (ICMAB-CSIC), 08193 Bellaterra, Catalonia, Spain*

Complete contact information is available at: https://pubs.acs.org/10.1021/acsomega.1c05352


### Notes

The authors declare no competing financial interest.

## ACKNOWLEDGMENTS

We acknowledge the funding of this research by FASTGRID Project (EU-H2020, 721019); the Projects COACHSUPENERGY (MAT2014-51778-C2-1-R) and SUMATE (RTI2018-095853-BC21 and RTI2018-095853-B-C22) from the Spanish Ministry of Economy and Competitiveness, which were cofunded by the European Regional Development Fund; and the Project 2017-SGR 753 from Generalitat de Catalunya and the COST Action NANOCOHYBRI (CA16218). ICMAB authors also acknowledge the Center of Excellence awards Severo Ochoa SEV-2015-0496 and CEX2019-000917-S.

## REFERENCES


(1) Obradors, X.; Puig, T. Coated Conductors for Power Applications: Materials Challenges. *Supercond. Sci. Technol.* **2014**, *27* (4), 044003.

(2) MacManus-Driscoll, J. L.; Wimbush, S. C. Processing and Application of High-Temperature Superconducting Coated Conductors. *Nat. Rev. Mater.* **2021**, *6* (7), 587−604.

(3) Awaji, S.; Watanabe, K.; Oguro, H.; Miyazaki, H.; Hanai, S.; Tosaka, T.; Ioka, S. First Performance Test of a 25 T Cryogen-Free Superconducting Magnet. *Supercond. Sci. Technol.* **2017**, *30* (6), 065001.

(4) Tixador, P. *Superconducting Fault Current Limiter*; World Scientific Series in Applications of Superconductivity and Related Phenomena; World Scientific, 2018; Vol. *03*. DOI: 10.1142/11062.

(5) Tixador, P.; Bauer, M.; Bruzek, C.-E.; Calleja, A.; Deutscher, G.; Dutoit, B.; Gomory, F.; Martini, L.; Noe, M.; Obradors, X.; Pekarcikova, M.; Sirois, F. Status of the European Union Project FASTGRID. *IEEE Trans. Appl. Supercond.* **2019**, *29* (5), 1−5.

(6) Moyzykh, M.; Gorbunova, D.; Ustyuzhanin, P.; Sotnikov, D.; Baburin, K.; Maklakov, A.; Magommedov, E.; Shumkov, A.; Telnova, A.; Shcherbakov, V.; Kumarov, D.; Sabirov, L.; Medovik, M.; Kadyrbaev, A.; Alexandrov, S.; Mikoyan, I.; Samoilenkov, S.; Vavilov, A. First Russian 220 KV Superconducting Fault Current Limiter (SFCL) for Application in City Grid. *IEEE Trans. Appl. Supercond.* **2021**, *31*, No. 5601707, DOI: 10.1109/TASC.2021.3066324.

(7) Higashikawa, K.; Inoue, M.; Ye, S.; Matsumoto, A.; Kumakura, H.; Yoshida, R.; Kato, T.; Machi, T.; Ibi, A.; Izumi, T.; Kiss, T. Scanning Hall-Probe Microscopy for Site-Specific Observation of Microstructure in Superconducting Wires and Tapes for the Clarification of Their Performance Bottlenecks. *Supercond. Sci. Technol.* **2020**, *33* (6), 064005.

(8) Jorgensen, J. D. Defects and Superconductivity in the Copper Oxides. *Phys. Today* **1991**, *44* (6), 34−40.

(9) Lao, M.; Bernardi, J.; Bauer, M.; Eisterer, M. Critical Current Anisotropy of GdBCO Tapes Grown on ISD−MgO Buffered Substrate. *Supercond. Sci. Technol.* **2015**, *28* (12), 124002.

(10) Gurevich, A. Thermal Instability near Planar Defects in Superconductors. *Appl. Phys. Lett.* **2001**, *78* (13), 1891−1893.

(11) Ekin, J. Example Calculations of Minimum Contact Area. In *Experimental Techniques for Low-Temperature Measurements*; Oxford University Press, 2006; pp 341−346. DOI: 10.1093/acprof:oso/9780198570547.001.0001.

(12) Bonura, M.; Senatore, C. Temperature and Field Dependence of the Quench Propagation Velocity in Industrial REBCO Coated Conductors. *IEEE Trans. Appl. Supercond.* **2017**, *27* (4), 1−5.

(13) Levin, G. A.; Novak, K. A.; Barnes, P. N. The Effects of Superconductor−Stabilizer Interfacial Resistance on the Quench of a Current-Carrying Coated Conductor. *Supercond. Sci. Technol.* **2010**, *23* (1), 014021.

(14) Bonura, M.; Senatore, C. An Equation for the Quench Propagation Velocity Valid for High Field Magnet Use of REBCO Coated Conductors. *Appl. Phys. Lett.* **2016**, *108* (24), 242602.

(15) Kudymow, A.; Noe, M.; Schacherer, C.; Kinder, H.; Prusseit, W. Investigation of YBCO Coated Conductor for Application in Resistive Superconducting Fault Current Limiters. *IEEE Trans. Appl. Supercond.* **2007**, *17* (2), 3499−3502.

(16) Colangelo, D.; Dutoit, B. Inhomogeneity Effects in HTS Coated Conductors Used as Resistive FCLs in Medium Voltage Grids. *Supercond. Sci. Technol.* **2012**, *25* (9), 095005.

(17) Awaji, S.; Hou, Y.; Oguro, H.; Watanabe, K.; Inoue, I.; Sakamoto, H.; Yasunaga, S.; Ryu, J. Hot Spot Behavior of Y123 Coated Conductors. *IEEE Trans. Appl. Supercond.* **2012**, *22* (3), 6601004−6601004.

(18) Fu, Y.; Tsukamoto, O.; Furuse, M. Copper Stabilization of YBCO Coated Conductor for Quench Protection. *IEEE Trans. Appiled Supercond.* **2003**, *13* (2), 1780−1783.

(19) Tixador, P.; Nguyen, N. T. Design of ReBaCuO-Coated Conductors for FCL. *Supercond. Sci. Technol.* **2012**, *25* (1), 014009.

(20) Tixador, P.; Badel, A. Superconducting Fault Current Limiter Optimized Design. *Phys. C Supercond. its Appl.* **2015**, *518*, 130−133.

(21) Wang, X.; Trociewitz, U. P.; Schwartz, J. Self-Field Quench Behaviour of YBa 2 Cu 3 O 7−$\delta$ Coated Conductors with Different Stabilizers. *Supercond. Sci. Technol.* **2009**, *22* (8), 085005.

(22) Levin, G. A.; Jones, W. A.; Novak, K. A.; Barnes, P. N. The Effects of Superconductor−Stabilizer Interfacial Resistance on




https://doi.org/10.1021/acsomega.1c05352
*ACS Omega* 2022, 7, 15315−15325

Quenching of a Pancake Coil Made out of Coated Conductor. *Supercond. Sci. Technol.* **2011**, *24* (3), 035015.
(23) Lacroix, C.; Fournier-Lupien, J. H.; McMeekin, K.; Sirois, F. Normal Zone Propagation Velocity in 2G HTS Coated Conductor with High Interfacial Resistance. *IEEE Trans. Appl. Supercond.* **2013**, *23* (3), 4701605.
(24) Lacroix, C.; Sirois, F. Corrigendum: Concept of a Current Flow Diverter for Accelerating the Normal Zone Propagation Velocity in 2G HTS Coated Conductors (2014 Supercond. Sci. Technol. 27 035003). *Supercond. Sci. Technol.* **2014**, *27* (12), 129501.
(25) Lacroix, C.; Sirois, F.; Wertheimer, M. R. Increased Normal Zone Propagation Velocity in Superconducting Segments. U. S. Pat. US20150045231A1, 2015.
(26) Lee, J.-H.; Lee, H.; Lee, J.-W.; Choi, S.-M.; Yoo, S.-I.; Moon, S.-H. RCE-DR, a Novel Process for Coated Conductor Fabrication with High Performance. *Supercond. Sci. Technol.* **2014**, *27* (4), 044018.
(27) Fournier-Lupien, J. H.; Lacroix, C.; Huh, J.; Masse, J. P.; Bellemare, J.; Sirois, F. Effect of Annealing on HTS Tapes with a Cerium Oxide Layer Inserted between the REBaCuO and Silver Layers. *Materialia* **2021**, *15*, 101029.
(28) Vilardell, M.; Fornell, J.; Sort, J.; Vlad, R.; Fernández, J.; Puig, J.; Usoskin, A.; Palau, A.; Puig, T.; Obradors, X.; Calleja, A. Inkjet-Printed Chemical Solution Y2O3 Layers for Planarization of Technical Substrates. *Coatings* **2017**, *7* (12), 227.
(29) Vilardell, M.; Granados, X.; Ricart, S.; Van Driessche, I.; Palau, A.; Puig, T.; Obradors, X. Flexible Manufacturing of Functional Ceramic Coatings by Inkjet Printing. *Thin Solid Films* **2013**, *548*, 489−497.
(30) Soler, L.; Jareño, J.; Banchewski, J.; Rasi, S.; Chamorro, N.; Guzman, R.; Yáñez, R.; Mocuta, C.; Ricart, S.; Farjas, J.; Roura-Grabulosa, P.; Obradors, X.; Puig, T. Ultrafast Transient Liquid Assisted Growth of High Current Density Superconducting Films. *Nat. Commun.* **2020**, *11* (1), 344.
(31) Fournier-Lupien, J. H.; Del Vecchio, P.; Lacroix, C.; Sirois, F. Analytical Model of 2D Electric Potential and Current Transfer in Superconducting Tapes with a Current Flow Diverter Architecture. *Supercond. Sci. Technol.* **2020**, *33* (11), 115014 DOI: 10.1088/1361-6668/aba543.
(32) Fournier-Lupien, J.-H.; Sirois, F.; Lacroix, C. Concepts of Static vs. Dynamic Current Transfer Length in 2G HTS Coated Conductors with a Current Flow Diverter Architecture. *Supercond. Sci. Technol.* **2021**, *34* (8), 085001.
(33) Prusseit, W.; Nemetschek, R.; Hoffmann, C.; Sigl, G.; Lümkemann, A.; Kinder, H. ISD Process Development for Coated Conductors. *Phys. C Supercond. its Appl.* **2005**, *426−431* (II), 866−871.
(34) Bauer, M.; Metzger, R.; Semerad, R.; Berberich, P.; Kinder, H. Inclined Substrate Deposition by Evaporation of Magnesium Oxide for Coated Conductors. *MRS Proc.* **1999**, *585* (1), 35.
(35) Metzger, R.; Bauer, M.; Numssen, K.; Semerad, R.; Berberich, P.; Kinder, H. Superconducting Tapes Using ISD Buffer Layers Produced by Evaporation of MgO or Reactive Evaporation of Magnesium. *IEEE Trans. Appiled Supercond.* **2001**, *11* (1), 2826−2829.
(36) Oh, S. S.; Kim, H. S.; Ha, H. S.; Ko, R. K.; Ha, D. W.; Lee, H.; Moon, S. H.; Yoo, S. I. Progress in Research and Development for REBCO Coated Conductors by Reactive Co-Evaporation. *Prog. Supercond. Cryog.* **2013**, *15* (4), 1−5.
(37) Vlad, V. R.; Usoskin, A.; Lee, S.; Petrykin, V.; Molodyk, A.; Bartolome, E.; Vilardell, M.; Calleja, A.; Meledin, A.; Obradors, X.; Puig, T.; Ricart, S.; Van Tendeloo, G. Inkjet Printing Multideposited YBCO on CGO/LMO/MgO/Y2O3/Al2 O3/Hastelloy Tape for 2G-Coated Conductors. *IEEE Trans. Appl. Supercond.* **2018**, *28* (4), 1−5.
(38) Minemawari, H.; Yamada, T.; Matsui, H.; Tsutsumi, J.; Haas, S.; Chiba, R.; Kumai, R.; Hasegawa, T. Inkjet Printing of Single-Crystal Films. *Nature* **2011**, *475* (7356), 364−367.
(39) Oxuolutia, S. L.; Lacroix, C.; Sirois, F. Method for Producing a Digital Inkjet Printing Ink, and Thus Obtained Digital Inkjet Printing Ink. EO Pat. 18382760.9; Higher Council for Scientific Research, 2017.
(40) Villarejo, B.; Pino, F.; Pop, C.; Ricart, S.; Vallès, F.; Mundet, B.; Palau, A.; Roura-Grabulosa, P.; Farjas, J.; Chamorro, N.; Yáñez, R.; Granados, X.; Puig, T.; Obradors, X. High Performance of Superconducting YBa2Cu3O7Thick Films Prepared by Single-Deposition Inkjet Printing. *ACS Appl. Electron. Mater.* **2021**, *3* (9), 3948−3961.
(41) Rasi, S.; Ricart, S.; Obradors, X.; Puig, T.; Roura, P.; Farjas, J. Thermal Decomposition of Yttrium Propionate: Film and Powder. *J. Anal. Appl. Pyrolysis* **2018**, *133*, 225−233.
(42) Granados, X.; Iliescu, S.; Bozzo, B.; Bartolome, E.; Puig, T.; Obradors, X.; Amorós, J.; Carrera, M. Magnetic Mapping - A Way to Test and Understand Current Flows in Thin and Bulk Superconductors. *Adv. Sci. Technol.* **2006**, *47*, 1−6.
(43) Farjas, J.; Camps, J.; Roura, P.; Ricart, S.; Puig, T.; Obradors, X. Thermoanalytical Study of the Formation Mechanism of Yttria from Yttrium Acetate. *Thermochim. Acta* **2011**, *521* (1−2), 84−89.
(44) TALLAN, N. M.; VEST, R. W. Electrical Properties and Defect Structure of Y2O3. *J. Am. Ceram. Soc.* **1966**, *49* (8), 401−404.
(45) Carrera, M.; Granados, X.; Amorös, J.; Maynou, R.; Puig, T.; Obradors, X. Detection of Current Distribution in Bulk Samples with Artificial Defects from Inversion of Hall Magnetic Maps. *IEEE Trans. Appl. Supercond.* **2009**, *19* (3), 3553−3556.
(46) Golodets, G. I. Chapter VII: The Dissociation of Molecular Oxygen, The Recombination of Oxygen Atoms and Isotopic Exchange with Molecular Oxygen. *Stud. Surf. Sci. Catal.* **1983**, *15*, 180−199.
(47) Merkle, R.; Maier, J. The Significance of Defect Chemistry for the Rate of Gas−Solid Reactions: Three Examples. *Top. Catal.* **2006**, *38* (1−3), 141−145.
(48) Cayado, P.; Sánchez-Valdés, C. F.; Stangl, A.; Coll, M.; Roura, P.; Palau, A.; Puig, T.; Obradors, X. Untangling Surface Oxygen Exchange Effects in YBa2Cu3O6+x Thin Films by Electrical Conductivity Relaxation. *Phys. Chem. Chem. Phys.* **2017**, *19* (21), 14129−14140.
(49) Stangl, A.; Palau, A.; Deutscher, G.; Obradors, X.; Puig, T. Ultra-High Critical Current Densities of Superconducting YBa2-Cu3O7-$\delta$ Thin Films in the Overdoped State. *Sci. Rep.* **2021**, *11* (1), 8176.


https://doi.org/10.1021/acsomega.1c05352
*ACS Omega* 2022, 7, 15315−15325